RESEARCH PAPER

Experimental and numerical investigations into flow features in an intake duct for the waterjet propulsion under mooring conditions

Renfang Huang[1] · Ruizhi Zhang[2] · Yiwei Wang[1,3] · Xianwu Luo[4] · Lei Zhu[5]

Abstract

The waterjet propulsion is widely applied in the marine vessels over 30 knots, and the intake duct is considered as an essential component that strongly relates to the propulsion performance. This paper sheds light on the flow features inside an intake duct under mooring conditions by using the particle image velocimetry (PIV) technique with three-dimensional (3D) numerical simulations. The hydraulic loss gradually increase as the flow-rate increases. According to analyses via the Bernoulli equation, the hydraulic loss is composed of the frictional head loss ($h_f \sim V^{1.75}$) and the local head loss ($h_j \sim V^{2.0}$). A recirculation region is observed near the duct lower wall with a high-velocity flow near the upper wall, and subsequently a shear flow presents in the horizontal straight pipe with an obvious velocity gradient. Three-dimensional simulations demonstrate that the vortex pair is very strong in the recirculation region and then it gradually decreases as the fluid flows downstream. With the flow-rate increasing, the non-uniformity at the duct outlet firstly increases to a peak and then slightly decreases, while the perpendicularity at the duct outlet dramatically decreases to a minimum and then increases. This work not only reveals some physics of the waterjet propulsion under mooring conditions, but also promotes its efficient operation.

Keywords Waterjet propulsion · Particle image velocimetry (PIV) · Intake duct · Waterjet pump · Mooring conditions

Abbreviations

CFD	Computational fluid dynamics
IVR	Inlet velocity ratio
JVR	Jet velocity ratio

NSGA-II	Non-dominated sorting genetic algorithm-II
PIV	Particle image velocimetry
RANS	Reynolds-averaged Navier-Stokes
RMS	Root mean square
a	Correction factor for the kinetic energy, $a = 1.05$–1.10
Q	Flow-rate
H	Pump head
H_n	Normalized helicity
h_w	Hydraulic loss
h_f	Frictional head loss
h_j	Local head loss
p	Pressure
Δp	Pressure difference, $\Delta p = p_1 - p_2$
u_i	i-th velocity
u_j	j-th velocity
V	Fluid velocity
V_{xy}	Velocity component at xy-plane
V_z	Velocity in z-direction
$\overline{V_z}$	Averaged velocity component in z-direction
z	Height
Ω'_x	Relative vorticity fields
Ω	Vorticity

✉ Yiwei Wang
wangyw@imech.ac.cn

✉ Xianwu Luo
luoxw@tsinghua.edu.cn

1 Key Laboratory for Mechanics in Fluid Solid Coupling Systems, Institute of Mechanics, Chinese Academy of Sciences, Beijing 100190, China

2 Science and Technology on Water Jet Propulsion Laboratory, Shanghai 200011, China

3 College of Engineering Science, University of Chinese Academy of Sciences, Beijing 100049, China

4 State Key Laboratory of Hydroscience and Engineering, Department of Energy and Power Engineering, Tsinghua University, Beijing 100084, China

5 China Institute of Water Resources and Hydropower Research, Beijing 100038, China

ρ Density
μ, μ_t Laminar and turbulent eddy viscosity
ξ Non-uniformity
φ_p Perpendicularity

1 Introduction

The waterjet propulsion has been widely applied in the marine vessel whose speed is over 30 knots due to its advantages such as high propulsive efficiency, good maneuverability, less vibration and noise, good anti-cavitation performance [1–4]. The intake duct is an essential component in the waterjet propulsion, since the water is inhaled through the intake duct, gets high kinetic energy from the waterjet pump, and then provides the thrust to the marine vessels. As a diversion component, about 7%–9% of the total energy is lost in the intake duct if there are unexpected flow patterns like flow separation and outflow non-uniformity [1, 2, 5]. Moreover, the waterjet-hull interaction mainly occurs near the suction entrance of the intake duct, and its effect on the propulsive efficiency is over 20% [6, 7]. Therefore, the intake duct plays an important role in the waterjet propulsion system, and many efforts have been made to investigate the intake duct from various aspects, i.e. the internal flow features, optimization design, the waterjet-hull interaction, etc.

Experimental fluid dynamics is a preferable approach to reveal physics [8–10]. A planning hull test boat is used to measure the pump loading parameters, the static pressure, the ingested hull boundary layer characteristics, etc. [11]. A scale waterjet intake duct model is mounted in a wind tunnel to study the dependence of the boundary layer thickness on the outflow quality [12]. Results show that the thickened boundary layer would cause more extensive flow separation, and the cut-water separation flows under maneuvering conditions would choke the inlet and suppress the available maneuvering thrust [12]. The pressure distributions on the duct surfaces are measured by pressure tabs at three values of jet velocity ratio (JVR), and the velocity fields are measured at the symmetry plane of a prototype waterjet model via the particle image velocimetry (PIV) technique [13]. A pair of counter-rotating vortices is visualized at the nozzle exit, and the flow inside the duct is faster near the lip than that near the upper wall [13]. A newly dynamometer is designed to collect the six force components and the non-uniform suction flow is generated by using a pipe bundle in the suction pipe [14]. The measurement results illustrate that effects of the suction non-uniformity on the energy performance and the hydrodynamic forces of the pump impeller. Early experiments are conducted in the wind tunnel by using pressure tabs and field visualization techniques. However, the physical properties of water and air are different. For example, the density and viscosity of water are larger than that of air, and

this causes larger drag and energy loss. Specially, the liquid water becomes vaporous water when the local pressure is lower than the saturated vapor pressure, which is known as cavitation and would cause the performance breakdown, but this cavitation phenomenon is not considered in the wind tunnel.

With the development of the computer science and technology, numerical simulation has gradually become a powerful approach for scientific research and has been widely used in various engineering applications [15–23]. Regarding the liquid water in the intake duct, internal flows are numerically studied by using the Reynolds-averaged Navier-Stokes (RANS) method together with wall functions, the calculated results achieve an acceptable accuracy and demonstrate that the inflow non-uniformity is caused by the accumulating vorticity [24]. Besides, Park et al. [25] also numerically studied the flow features and the energy performance for a waterjet propulsion system by using the incompressible RANS method together with a sliding multi-block technique. Young et al. [26] numerically studied internal flows in a fully-coupled SES-waterjet system and the results demonstrate that the non-uniformity would cause load fluctuations and the unsteady cavitation [26]. This has also been confirmed by Duerr and von Ellenrieder [27]. Dependence of the pump performance on the non-uniform suction flow is numerically studied by Cao et al. [28], and results indicate that the large inflow non-uniformity is characterized by a distinct swirl distortion and this would cause a dramatic drop in the pump head. Energy performance of an intake duct is numerically analyzed at various values of inlet velocity ratio (IVR), illustrating the cavitation is likely to occur at the upper side of the duct cutwater and the duct hydraulic efficiency is firstly increased and subsequently followed by a drop with an increase in IVR [29]. Guo et al. [30] conducted the self-propulsion computations of a trimaran and developed a prediction tool to obtain the capture area via tracking the streamlines upstream. The results demonstrate that the resistance increment and the waterjet thrust deduction fraction always have different signs and the total efficiency is strongly related to the ideal jet efficiency and the pump efficiency. Zhao et al. [31] numerically and experimentally investigated cavitating flow characteristics in an axial flow waterjet pump and revealed that the cavitation process not only affects the blade loading but also relates to the incidence angle at the leading edge which is responsible for the flow structures on the suction surface. Effects of the stabilizer fins on dynamics around a waterjet-propelled ship are numerically studied by model-scale and full-scale transient simulations, and the results indicate that stabilizer fins would change the turbulent boundary layer distribution around the hull and even affect the capture area of the waterjet [32]. The hull-waterjet interaction for a planning trimaran is numerically studied and discussed the thrust deduction

and interaction efficiency in the speed range of $0.32 < Fr_L < 2.87$ [33].

Besides, the numerical simulation is widely applied to optimize the duct since it can not only rapidly give an acceptable result but also save the manufacturing cost as well as time. Effects of the inlet grids on the duct performance are numerically studied by comparing the duct with no grids, three grids and eight grids, and the results indicate that the inlet grids would cause a decrease in the performance of the duct and the waterjet propulsion [34]. The optimal setting angle of the grids is suggested to be 5° based on Luo's research [35], and the duct lip is recommended to be a more forward position with a sharper configuration for a better hydrodynamic performance based on the investigation by Liu and Huang [36]. The inclination angle of the intake duct is discussed via numerical simulations and the results show that the duct efficiency is gradually decreased as the inclination angle increases [37, 38]. A parametric design method is proposed to design the intake duct and then the computational fluid dynamics (CFD) technique is applied to predict the duct performance such as the uniformity, flow separations, energy performance and hydraulic loss [39]. Subsequently, the non-dominated sorting genetic algorithm-II (NSGA-II) is incorporated with the parametric design method and CFD technique to conduct the multi-objective optimization for the intake duct [1]. Guo et al. [40] conducted a multi-objective optimization of a waterjet-propelled trimaran with considering the waterjet-hull interaction, which is decomposed into the optimization of the waterjet system, the global hull shape, the local hull shape and the arrangement of the waterjet.

A brief review above demonstrates that the energy performance and internal flow features inside intake duct have been studied at specified vessel speeds by using both numerical and experimental approaches. Besides, the intake duct is also operated under mooring conditions (zero vessel speed) when the marine vessel docks at the pier. However, we still have inadequate understandings on the whole flow features in the intake duct under such mooring conditions. In this paper, a water tank is built up and used to conduct experiments for a duct model under mooring states. Based on PIV observations, the numerical simulation is adopted to illustrate three-dimensional flow features in the model-scale duct. This paper is organized as follows. The experimental approach and numerical simulation method are described in Sects. 2 and 3, respectively. Section 4 discusses the hydraulic loss, the planar velocity fields obtained by experiments and three-dimensional flow patterns calculated by numerical simulation. Last is the conclusions.

2 Experimental approach

The experiments are conducted to capture the velocity fields inside a model-scale duct and to measure the pressures under mooring conditions. The study is conducted at China Institute of Water Resources and Hydropower Research. The experimental apparatus is shown in Fig. 1, mainly including a water tank, an experimental model, PIV system and measurement system.

The water tank is 1236 mm × 524 mm × 650 mm (length × width × height) with a free surface. The water is driven by an ISW65-100IA centrifugal pump with the rated discharge of 44 m³/h and the rated head of 10 m. A ball valve is mounted at the pump outlet pipe to adjust the flow-rate during the operation. Note that there are small ball valves at the bottom of the pump, the inlet pipe and the outlet pipe to discharge the residual water after each experimental run.

The experimental model is an intake duct, which is made of the photosensitive resin composites by 3D printing technique and polish to a smooth finish. The scale of the duct model is 1:4.88. Figure 2 shows geometrical parameters of the intake duct, and the characteristic diameter is $D = 50$ mm. The inhaling water flows towards the $+z$ direction. The vertical and spanwise directions are designated by y-axis and x-axis, respectively.

Two YH203 pressure transducers are employed on the duct upper wall to measure the pressures under various flow-rates. A YH-3051DP differential pressure transducer is used to measure the differential pressure between the pump outlet and inlet, and then the actual pump head is calculated. The pressure transducers are calibrated before experiments by using a piston gauge according to the JJG 882-2004 pressure transducer standard (PTS). The uncertainty of the YH203 pressure transducers is ±0.5%, its frequency response range is 0–10 kHz with its natural frequency of 1×10^6 Hz. The uncertainty of the YH-3051DP differential pressure transducer is ±0.2%. The flow-rate is measured by an AXF065G-E2AL1S-BD11-41B electromagnetic flowmeter, and it is installed at the pump outlet pipe. The uncertainty of the electromagnetic flowmeter is ±0.35%.

The PIV system is composed of a computer, laser and charge coupled device (CCD) cameras. A Nd: YAG double-cavity laser is used to illuminate the flow field with the output energy of 200 mJ and wavelength of 532 nm. The laser sheet is overlapped with the midplane of the intake duct, which is generated by a laser probe from the bottom up. The thickness of the laser sheet is about 2 mm. The tracer particles in water are glass hollow spheres with a mean diameter of 10 μm. The particle traceability is evaluated by the Stokes number $St = \tau_p/\tau_f$, where τ_p is the particle response time and τ_f is the turbulence time scale of water. $St < 1$ indicates the particle traceability is good enough to visualize the flow
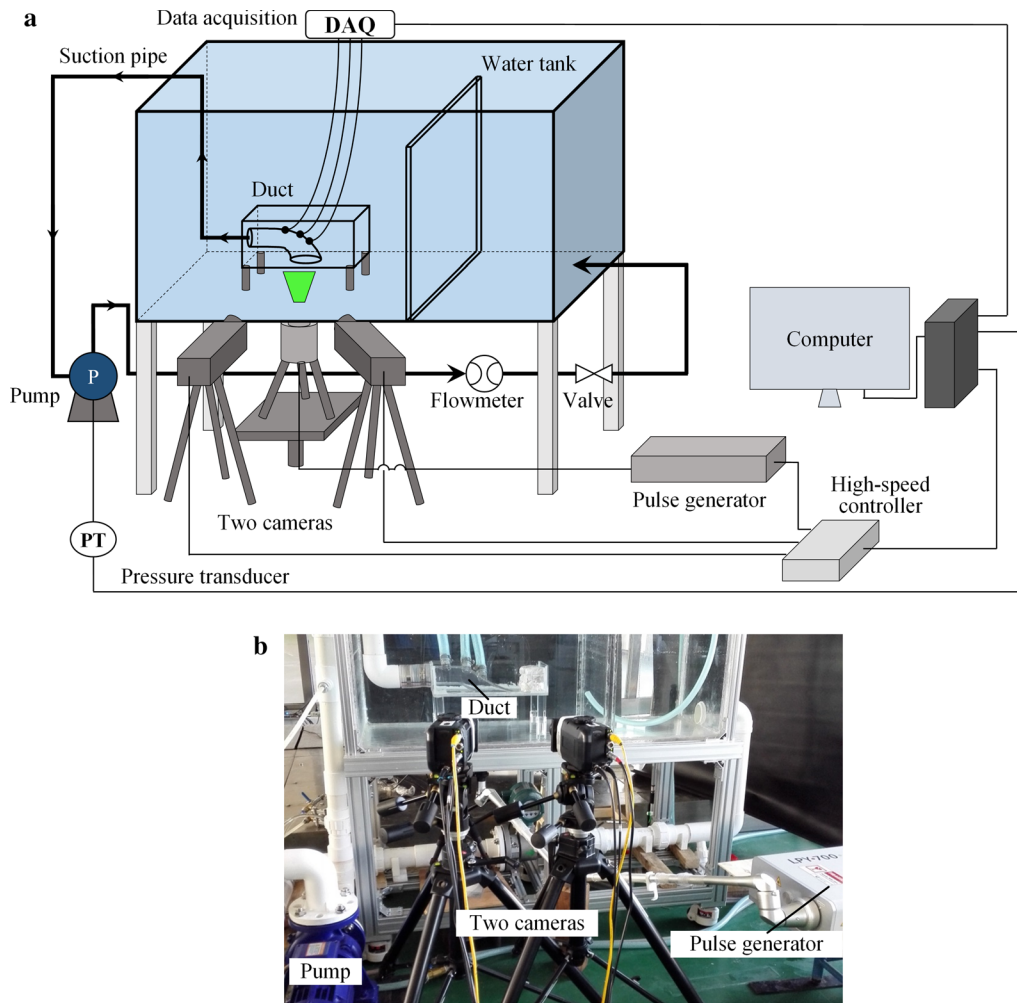
Fig. 1 Experimental apparatus for the intake duct including a water tank, particle image velocimetry (PIV) system and measurement system: **a** schematic diagram and **b** the on-site facility
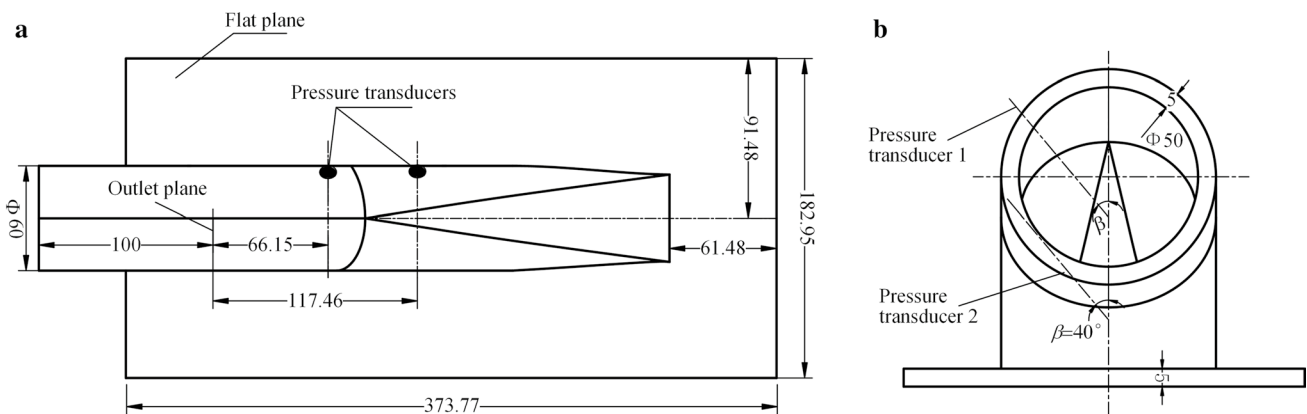

Fig. 2 Intake duct model and the pressure transducer arrangement: **a** top view and **b** side view (unit: mm)

features. In our PIV experiments, the corresponding Stokes number is $St = 0.0049\text{–}0.2165$. The St values are smaller than 1, demonstrating that the hollow glass spheres meet the St requirement of tracer particles.

Two imager LX 8M CCD cameras (12 bit digital) are used to capture the particle images with the spatial resolution of 3312×2488 pixels. Since the light intensity is quite different inside and outside the duct, so the flow field of the midplane is divided into two regions to obtain high spatial-resolution particle images, i.e. Region 1 in red dash line and Region 2 in blue dash line as shown in Fig. 3a. Therefore, Region 1 focuses on the flow field outside the duct, and Region 2 focuses on the flow features inside the duct. The planar flow fields in two regions have been measured separately with the flow-rate ranging from 2 to 25 m³/h. With the flow-rate increasing, the flow velocity becomes higher, the particle movement between two light pulses is increased, so it is necessary to gradually decrease the parameter σ (the time interval between two laser pulses) to avoid the tracer particles moving too much between two light pulses. The purpose is to ensure the accuracy of PIV measurement. Experimental conditions and corresponding parameter σ are listed in Table 1. The distance from the measurement plane to the cameras is around 500 mm as illustrated in Fig. 3b.

The overall procedure is described as follows:

1. Degassing. Since the air in water can be illuminated and recorded as seeding particles, this would cause the experimental error. To avoid the experimental error caused by the air, it is necessary to eliminate the air from the experimental system at the beginning of each test.
2. Calibration. A calibration plate is used to calculate the relationship between the image coordinates and the physical coordinates, where the black dots with an interval of ten millimeters are located on a white background. The plate shape fits well with the midplane of the intake duct.

Table 1 Experimental conditions

Q (m³/h)	σ (µs)
2	1500
4	760
6	520
8	380
10	320
12	220
14	185
16	160
20	150
25	120

3. Particle image recording. Cameras are set as the double-frame and double-pulse mode. The sampling rate is 100 Hz, and 400 frames are captured at each flow-rate. One pulse is set to 60% of the rated energy, and another pulse is set to 75%. Meanwhile, pressure data measured by the pressure transducers, and particle images are collected and stored in a computer.
4. Processing. As shown in Fig. 4a, the light intensity near the duct surface wall is much higher than that of the background, and this causes a bad velocity calculation. To solve this issue, a time filter is adopted to preprocess those particle images. The distribution of the minimum light intensity is calculated among n source images (n is filter length, herein $n = 5$), and the processed particle image is obtained by subtracting the corresponding minimum value from each raw image. Figure 4b shows the particle image processing with the time filter. The light intensity is approximately the same on the particle image. The stereo cross-correlation method together with the multi-pass iterations is used to calculate the velocity fields. The initial interrogation window is 64×64 pixels, the final interrogation window is 32×32 pixels, and the overlap of both interrogations are 50%. Therefore, we can obtain about 4700 velocity vectors
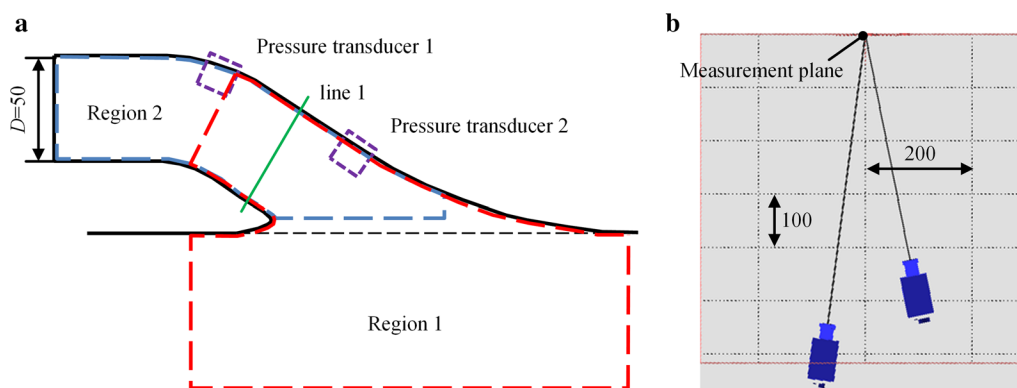

Fig. 3 **a** Measured regions for the intake duct and **b** the camera configurations (unit: mm)
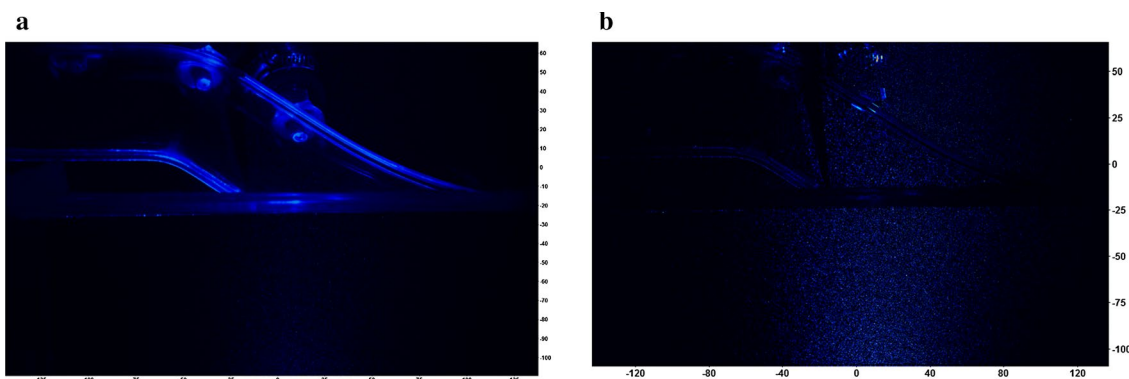
Fig. 4 Particle image: **a** without the time filter and **b** with the time filter

with 1.76 mm spacing for "Region 1" and 1600 velocity vectors for "Region 2". Take $Q = 10$ m³/h for instance, the typical particle image displacement is 3.5 pixel, the maximum velocity gradient is 0.07 pixels/pixel, and the general velocity gradient is 0.02 pixels/pixel. Therefore, the uncertainty in the planar velocity component is about 6%.

3 Numerical simulation method

Numerical simulation is used to give a better understanding for the three-dimensional flows inside the intake duct. The continuity and momentum equations are expressed as follows,

$$\frac{\partial \rho}{\partial t} + \frac{\partial (\rho u_j)}{\partial x_j} = 0, \tag{1}$$

$$\frac{\partial (\rho u_i)}{\partial t} + \frac{\partial (\rho u_i u_j)}{\partial x_j} = -\frac{\partial p}{\partial x_i} + \frac{\partial}{\partial x_j}\left[(\mu + \mu_t)\left(\frac{\partial u_i}{\partial x_j} + \frac{\partial u_j}{\partial x_i}\right)\right], \tag{2}$$

where ρ is the density, p is the pressure, u_i is the i-th velocity, u_j is the j-th velocity, μ and μ_t is the laminar and turbulent eddy viscosity. The re-normalisation group (RNG) k-ε turbulence model is adopted to closure the governing equations, which provides an analytically-derived differential formula for eddy viscosity and is suitable for both high-Reynolds number flows and low-Reynolds number flows [41].

The computational domain is made up of the intake duct, the large water tank, the inlet pipe and the outlet pipe. Present numerical simulations are not considered effects of the centrifugal pump. When it comes to the boundary conditions, the mass-flow-rate is set at the inlet, and the averaged static pressure is set at the outlet with the value measured from experiments. Free surface is set at the top of the water tank. No-slip wall is set at the other solid walls and the scalable wall function is used to solve the near wall flows. Three-dimensional flows inside the intake duct are calculated using the commercial software ANSYS CFX. Water at 25 °C is used as the liquid in the simulation, whose density is 997 kg/m³ and dynamic viscosity is 8.899×10^{-4} kg·m⁻¹·s⁻¹. The convergence residual is less than 1×10^{-5}.

Hybrid grids are meshed for the whole computational domain. Unstructured grids are meshed in the intake duct and structured grids are meshed in the other computational parts. Mesh details around the intake duct are shown in Fig. 5.

Three grids in the intake duct are created with a constant grid refinement ratio $r = 1.3$ in all three directions, the total element in the whole computational domain are quantified in Table 2. The discretization uncertainty is evaluated with the factor of safety (FS) method [42] by monitoring the non-uniformity (ξ) and perpendicularity (φ_p) at the duct outlet, i.e. Plane 6. The non-uniformity ξ and perpendicularity φ_p are defined in Eqs. (3) and (4), where V_z is the velocity in z-direction, $\bar{V}_z$ is the averaged velocity component in z-direction, V_{xy} is the velocity component at xy-plane. Plane 6 is the outlet plane of the intake duct, as shown in Fig. 6

$$\xi = \frac{1}{Q} \int\limits_{dA} \left| V_z - \overline{V_z} \right| dA, \tag{3}$$

$$\varphi_p = \frac{1}{Q} \int\limits_{dA} V_z \left[90° - \arctan\left(\frac{V_{xy}}{V_z}\right) \right] dA. \tag{4}$$
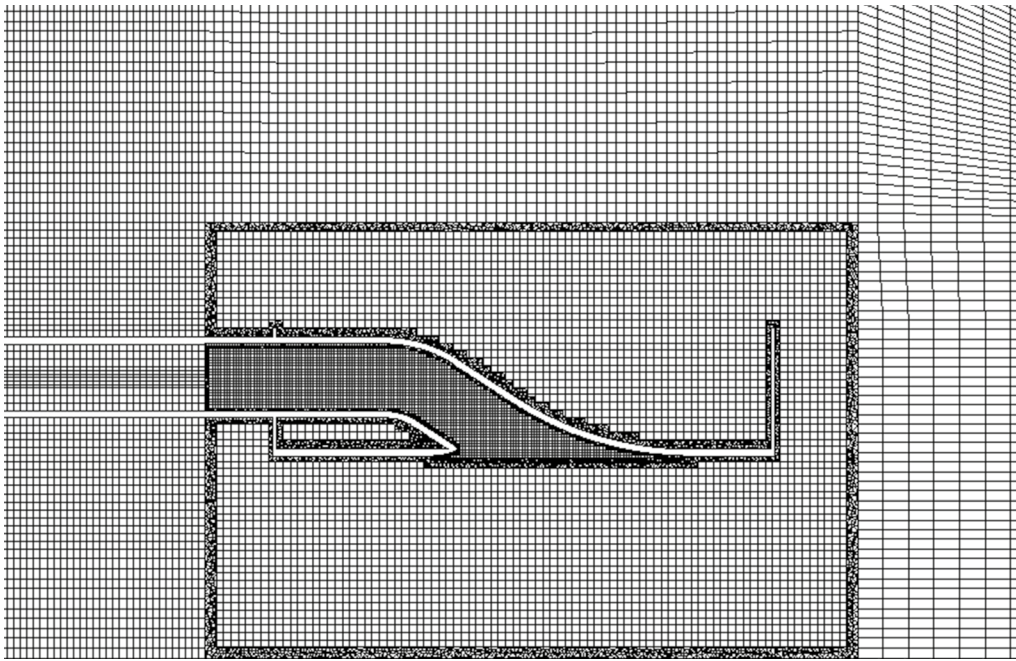
Fig. 5 Mesh for the intake duct

Table 2 Discretization uncertainty of non-uniformity (ξ) and perpendicularity (φ_p) at the duct outlet, i.e. Plane 6

Mesh	Grid quantities	ξ	φ_p
Fine	2,969,402	79.769	64.2272
Middle	2,118,331	79.2583	64.7303
Coarse	1,917,983	80.1958	65.0632
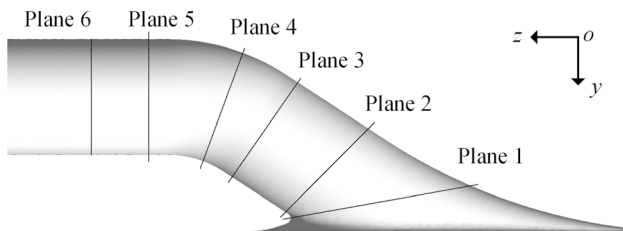
Fig. 6 Cross-section positions of the intake duct

As shown in Table 2, the uncertainty estimated by FS method is 7.57% for the non-uniformity and 9.26% for the perpendicularity, demonstrating that the simulation results are not sensitive to the grid resolution. Note that further grid refinement will lead to substantial increasing of computational cost and simulation instability [43]. Thus, the middle mesh is determined as the final mesh with 2,118,331 elements.
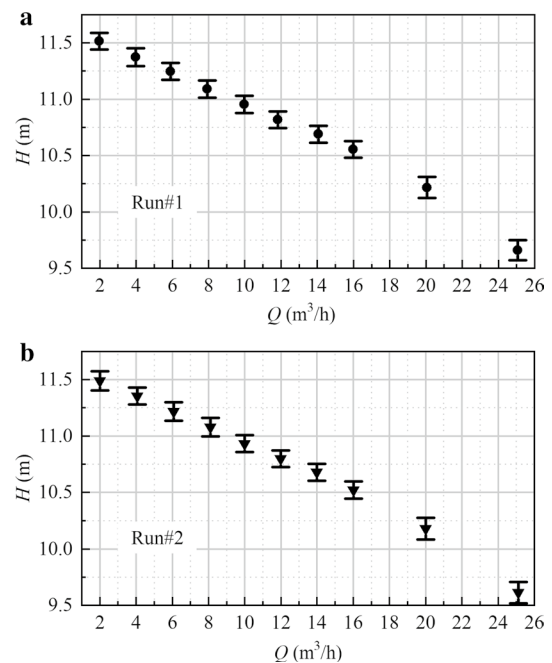
Fig. 7 Experimental conditions at **a** Run#1 and **b** Run#2

4 Results and discussions

4.1 Hydraulic loss in the intake duct

As depicted in Fig. 7, the experimental conditions are conducted at two runs. The flow fields in Region 1 are measured

at Run#1 with $Q = 2–25$ m³/h, and the flow fields in Region 2 are measured at Run#2 with $Q = 2–25$ m³/h. The operation conditions are almost the same at both Run#1 and Run#2. The pump head (H) is gradually decreased as the flow-rate (Q) increases. The maximal standard deviation of the pump head is 0.091 m at Run#1 and 0.096 m at Run#2. Therefore, the entire experimental apparatus generally runs stably with high reliability during $Q = 2–25$ m³/h.

Figure 8a shows the measured and simulated pressures at various flow-rates. The measured pressure at Run#1 is the same with that at Run#2. When compared with the numerical simulation, the measured p_1 is in pretty good accordance with the simulated p_1. On the other hand, there are discrepancies in p_2 between the numerical simulation and the experiment, although the variation tendency is the same. Both p_1 and p_2 are gradually decreased as the flow-rate (Q) increases. Applying the Bernoulli equation to p_1 and p_2, it comes to Eq. (5), where V, p, z is the fluid velocity, pressure, height, respectively; h_w is the hydraulic loss, including the frictional head loss h_f and the local head loss h_j; a is the correction factor for the kinetic energy, $a = 1.05–1.10$; subscript

1 and 2 correspond to the location of pressure transducer 1 and pressure transducer 2

$$z_1 + \frac{p_1}{\rho g} + \frac{a_1 V_1^2}{2g} = z_2 + \frac{p_2}{\rho g} + \frac{a_2 V_2^2}{2g} + h_w. \qquad (5)$$

Therefore, $\Delta p = p_1 – p_2$ is the pressure difference between the two pressure transducers, including the difference in the potential energy, the kinetic energy and the hydraulic loss, as expressed in Eq. (6),

$$\Delta p = (p_1 - p_2) = \rho g (z_2 - z_1) + \rho \left(\frac{a_2 V_2^2}{2} - \frac{a_1 V_1^2}{2} \right) + h_w. \qquad (6)$$

The Reynolds numbers range in $1.39 \times 10^4 – 1.77 \times 10^5$, the relative roughness factor of the material and the manufacturing process is around 3×10^{-4}. Based on previous studies [44], the flow inside the intake duct is turbulent and the frictional head loss h_f is proportional to $V^{1.75}$, i.e., $h_f \sim V^{1.75}$. Besides, the local head loss h_j is proportional to the square of the flow-rate, so it can be written as $h_j \sim V^{2.0}$. Therefore, the hydraulic loss h_w is made up of the frictional head loss ($h_f \sim V^{1.75}$) and the local head loss ($h_j \sim V^{2.0}$).

Ignore the position difference, Eq. (6) is simplified as,

$$\Delta p \approx \rho \left(\frac{a_2 V_2^2}{2} - \frac{a_1 V_1^2}{2} \right) + h_w \rightarrow V^2 + V^{1.75}. \qquad (7)$$

Figure 9 shows the variations of pressure difference (Δp) over the flow-rate (Q). With increasing the flow-rate, the pressure difference (Δp) by experiments is gradually increased, which can be fitted by Eq. (8) and plotted in blue curve in Fig. 9. The theoretical predictions by Eq. (8) is very close to the experimental data, and the root mean square (RMS) between the measured data and the theoretical predicted value is 9.4062
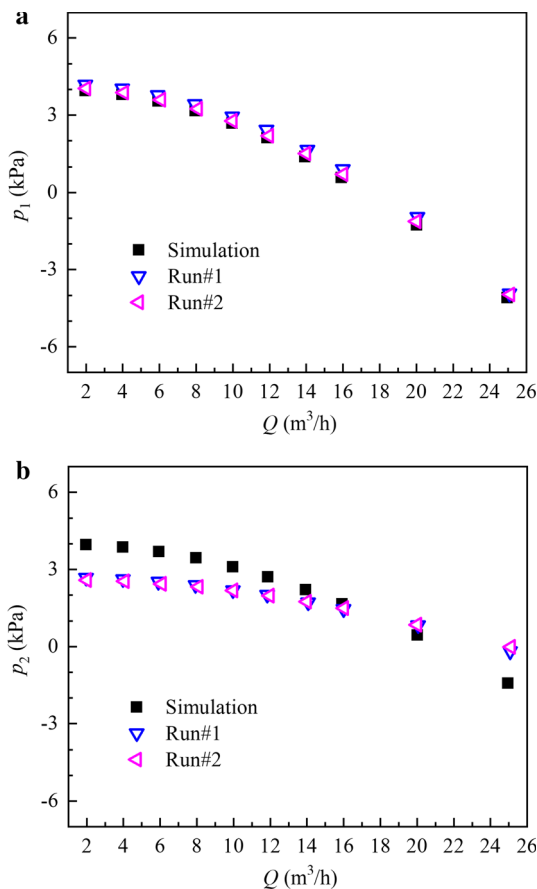

Fig. 8 Measured and simulated pressures at **a** pressure transducer 1 and **b** pressure transducer 2
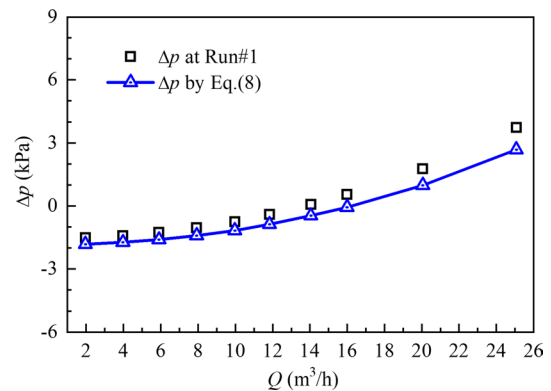

Fig. 9 Variations of pressure difference (Δp) at Run#1 and the hydraulic loss h_w over the flow-rate (Q)

$$\Delta p = 9.142Q^2 - 4.412Q^{1.75} + C. \tag{8}$$

4.2 Flow features at the midplane by PIV technique

As "Region 1" and "Region 2" are measured in two experiments, it is necessary to check whether velocity fields in the two regions match well or not. Herein, velocity profile on line 1 is extracted from the PIV measurement, noting that line 1 is located in the overlap region of the two regions (Fig. 3). Besides, the simulated velocity on line 1 is used for comparisons. As shown in Fig. 10, the results indicate that the high velocity near the upper wall and the lower velocity near the lip of intake duct are obtained by two measurements as well as present numerical simulations. Basically, it is confirmed that velocity fields in the two regions can match well, and the numerical simulation performs well to capture the velocity profile on line 1.

Figure 11 shows the time-averaged velocity distributions measured by the PIV technique in Region 1. When the flow-rate is varied from $Q = 2$ m³/h to $Q = 25$ m³/h, the flow structure is almost similar in Region 1. The fluid is mainly inhaled from the lower left of the intake duct, and the fluid velocity presents a uniform distribution outside the duct, which is also reported in Ref. [25]. The fluid flows into the duct due to its guidance effects. A flow separation is represented as a low-velocity zone near the duct lip. As a result, the effective flow area inside the intake duct is reduced, and the fluid near the duct upper wall is accelerated with an obvious velocity gradient from the duct upper wall towards the lower wall. Due to the fluid viscosity, the high-velocity fluid drives the low-velocity fluid and moves along the streamwise direction together.

Figure 12 shows time-averaged velocity distributions measured by the PIV technique in Region 2. The flow inside the intake duct can be completely illustrated since Region 2 includes the elbow section of the duct and the horizontal
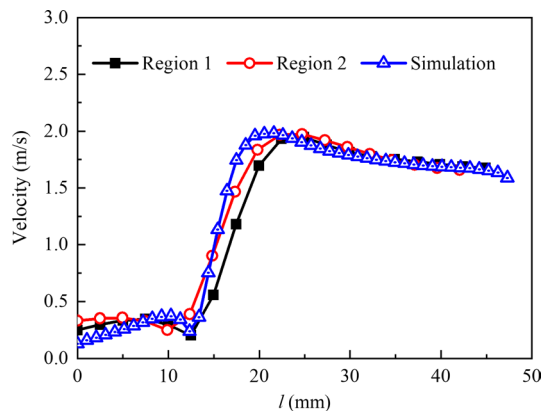
straight section. As shown in Fig. 12, there is another low-velocity zone near the pressure transducer 1, whose velocity is much larger than that near the duct lip. This may be caused by the impact of the upper wall on the fluid when the water flows through the elbow. Besides, the low-velocity separation flow and the high-velocity flow are clearly observed by the PIV technique. As the fluid further flows downstream, the flow separation disappears and meanwhile a shear flow exists in the horizontal straight section with an obvious velocity gradient from the duct upper wall towards the lower wall. This indicates the intake duct is characterized by the outflow non-uniformity which strongly affects the pump performance at the downstream based on the previous investigation [18] .

Relative vorticity fields (Ω'_x) in Region 2 are illustrated in Fig. 13. In the range of $Q = 2$–25 m³/h, the vorticity features stay unchanged in Region 2. The separation flow presents very low vorticity, and there is positive-vorticity zone above the separation flow, which forms a vortex pair near the duct lip. The zone of the vortex pair is gradually increased with the flow-rate. Besides, the vorticity is close to zero near the upper wall, indicating that the secondary flow along x-axis is very small near the duct upper wall.

The normalized helicity (H_n) is introduced to analyze the interaction between the vorticity and the velocity. It is defined in Eq. (9), where $\boldsymbol{\Omega}$ is the vorticity, $\boldsymbol{\Omega} = \nabla \times \boldsymbol{V}$, H_n is the normalized helicity ranging from -1 to $+1$. If the normalized helicity is positive, the vorticity and the velocity is in the same direction, so the vortex is enhanced. In contrast, the negative helicity demonstrates the vorticity and the velocity is in opposite direction, so the vortex is suppressed. As shown in Fig. 14, the normalized helicity presents a similar distribution with increasing the flow-rate. The normalized helicity is positive near the upper wall, while it has negative values in the middle of the flow passage, demonstrating the vortex is promoted along with the water suction process and this will be depicted from the three-dimensional perspective in Sect. 4.3

$$H_n = \frac{\boldsymbol{V} \cdot \boldsymbol{\Omega}}{|\boldsymbol{V}||\boldsymbol{\Omega}|}. \tag{9}$$

4.3 Simulated flow fields inside the intake duct

Based on the pressure analysis in Fig. 8, the simulated pressure is in good agreement with the experiments. There is a small discrepancy in the p_2 value between simulations and experiments, but it is permitted in engineering practices. The calculated flow fields are shown in Fig. 15 and compared with the PIV results. It is indicated the numerical simulation can well predict those flow features including the velocity gradient inside the duct, the separation flow near
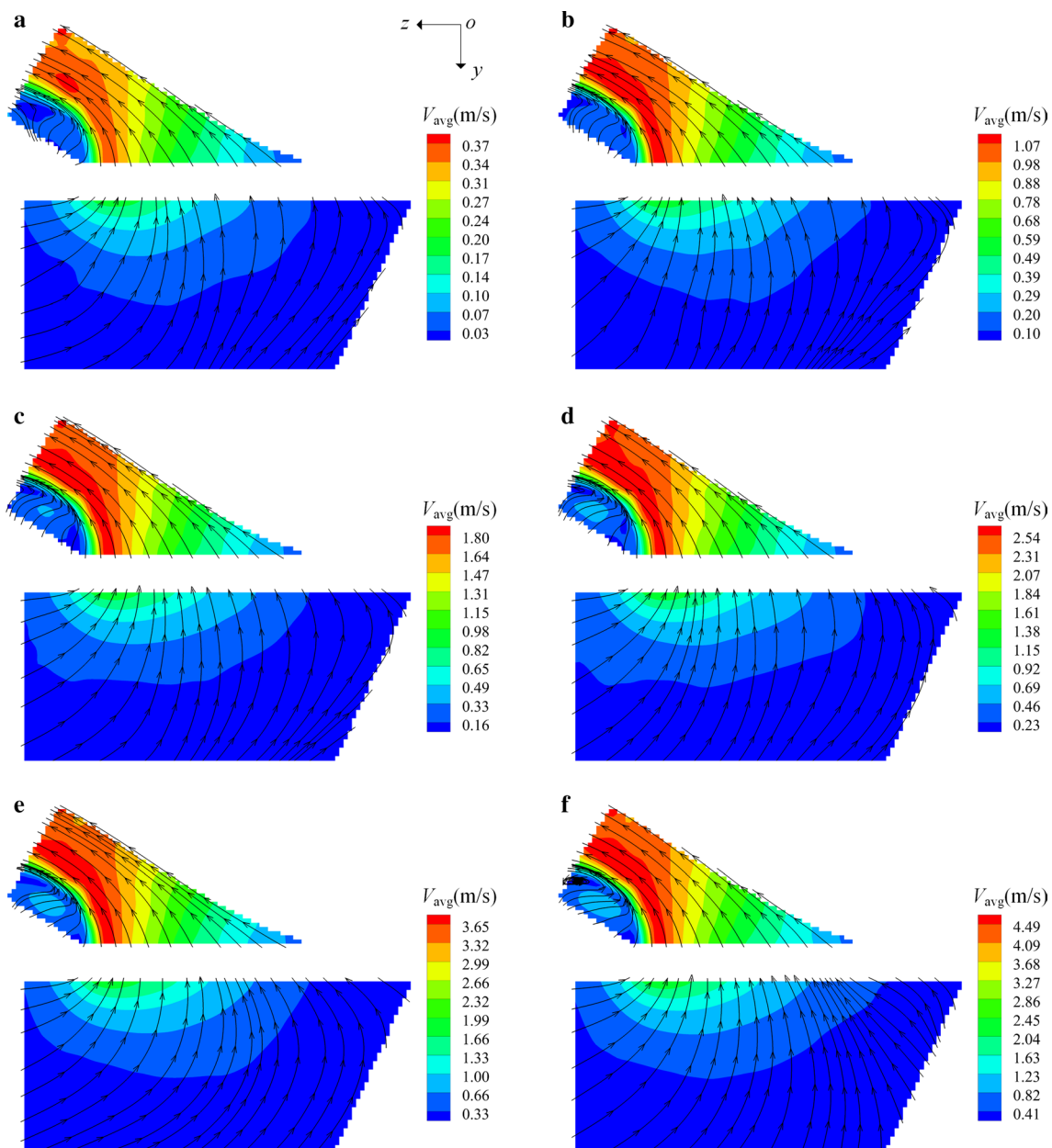

Fig. 10 Velocity comparisons on line 1 ($Q = 10$ m³/h)

Fig. 11 Time-averaged velocity distributions measured by the PIV technique in Region 1. **a** $Q = 2$ m³/h, **b** $Q = 6$ m³/h, **c** $Q = 10$ m³/h, **d** $Q = 14$ m³/h, **e** $Q = 20$ m³/h, **f** $Q = 25$ m³/h

the lower wall and the high-velocity flow near the upper wall, and those features are in good accordance with those observed in experiments. Both the numerical simulation and the PIV approach mutually demonstrate the flow patterns at the midplane of the intake duct as shown in Fig. 16. The fluid is mainly inhaled from lower left side below the intake duct. Subsequently, it strikes the duct upper right wall and separates to form two streams with a stagnation point. Two streams are in the opposite directions, one is drawn into the

duct and the other continually flows towards the right side. The drawn flow is separated into a recirculation region near the lower wall and a high-velocity flow near the upper wall, and finally forms a shear flow in the horizontal straight pipe with an obvious velocity gradient.

The three-dimensional flows inside the duct are depicted at five cross-sections in Fig. 6. Plane 1 is near the suction inlet; Plane 4 is around the elbow position and Plane 5 is in the horizontal straight pipe. The velocity distributions
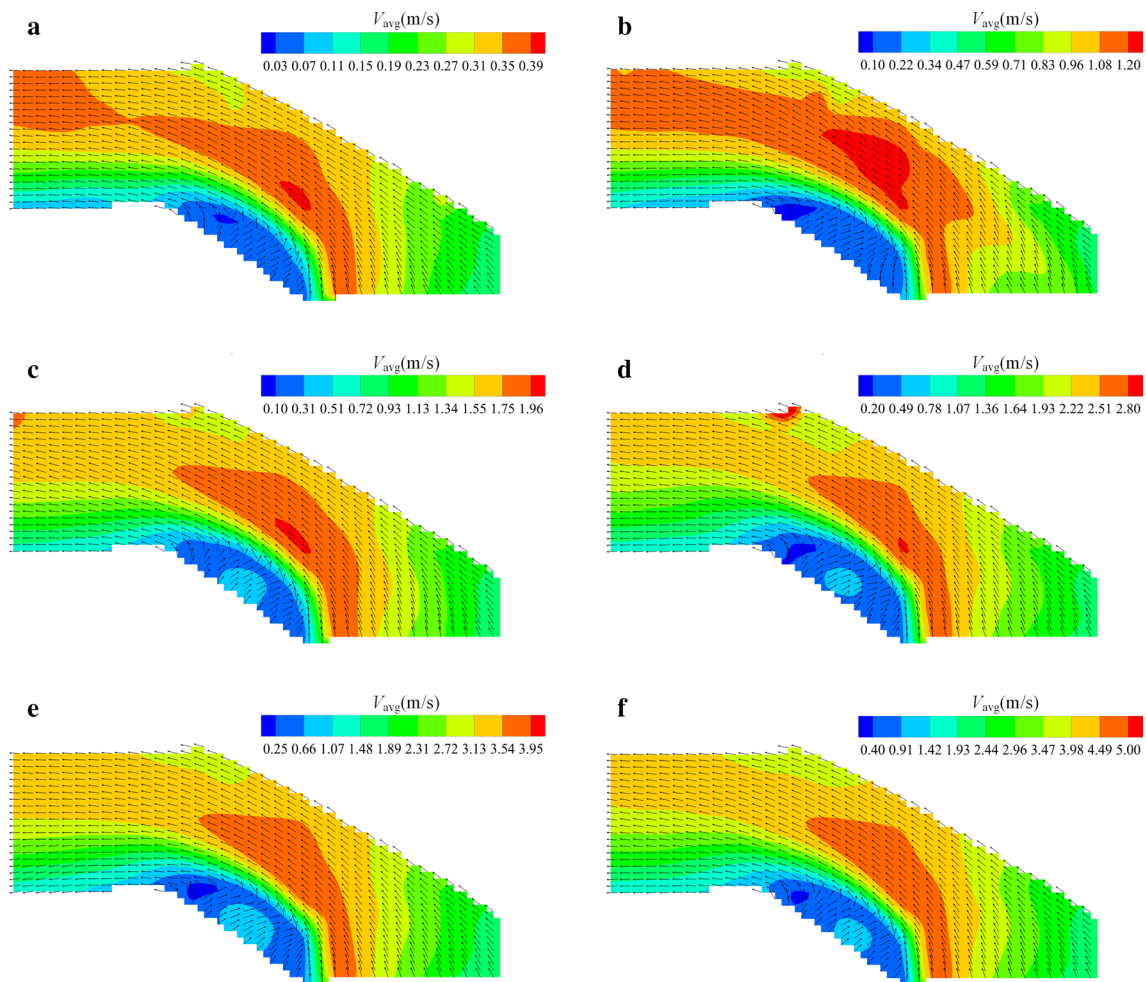
Fig. 12 Time-averaged velocity distributions measured by the PIV technique in Region 2. **a** $Q = 2$ m^3/h, **b** $Q = 6$ m^3/h, **c** $Q = 10$ m^3/h, **d** $Q = 14$ m^3/h, **e** $Q = 20$ m^3/h, **f** $Q = 25$ m^3/h
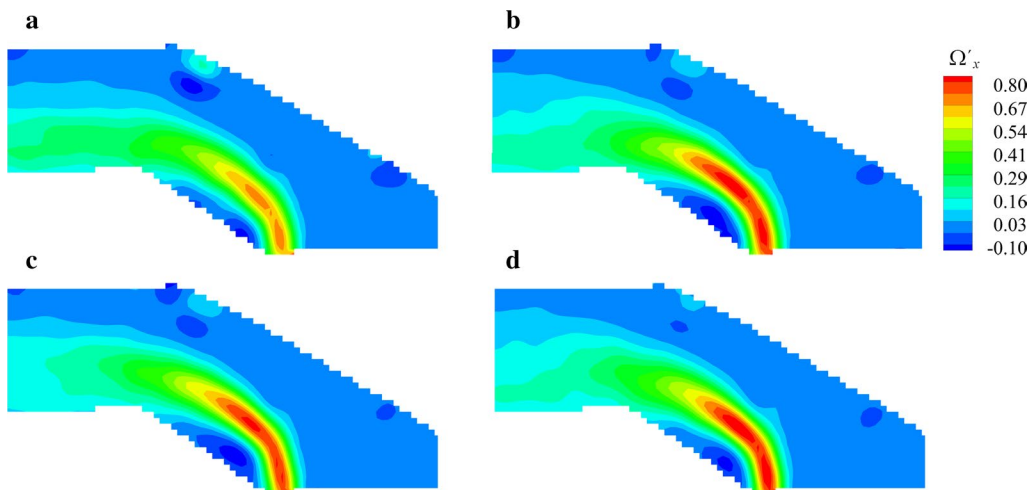
Fig. 13 Relative vorticity fields (Ω'_x) in Region 2. **a** $Q = 2$ m^3/h, **b** $Q = 10$ m^3/h, **c** $Q = 16$ m^3/h, **d** $Q = 25$ m^3/h

H_n

-0.90 -0.60 -0.30 0.00 0.30 0.60 0.90
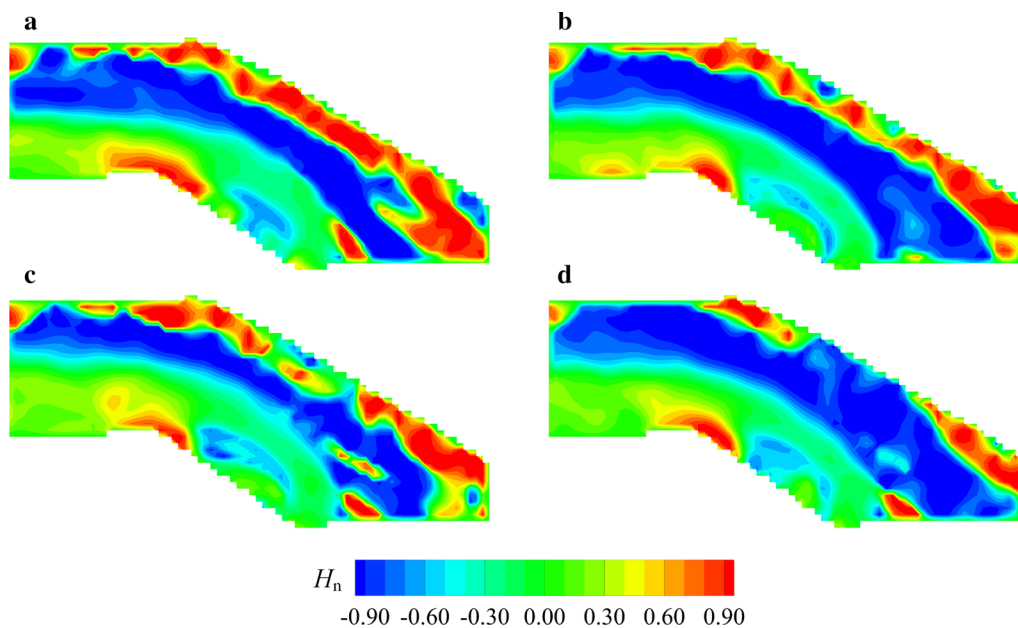
Fig. 14 Normalized helicity (H_n) distributions in Region 2. **a** $Q = 2$ m³/h, **b** $Q = 10$ m³/h, **c** $Q = 16$ m³/h, **d** $Q = 25$ m³/h

and streamlines at various cross-sections are depicted in Fig. 17. There is a clearly velocity gradient from the upper wall towards the lower wall, and the velocity distribution is axisymmetric at those cross-sections. The streamlines at Plane 1 demonstrate that the flow is mostly drawn into the duct from the lower left side. Due to the existence of the recirculation region in the inclined straight section, a vortex pair is observed at Plane 3. Subsequently, when the flow strikes the upper wall in the elbow section, two vortex pairs are observed at Plane 4, and then the flow is very complex at Plane 5. The vortex pair is very strong in the recirculation region and then it gradually decreases along with the fluid flowing downstream.

The outflow quality is quantified by the non-uniformity ξ and perpendicularity φ_p. Figure 18 shows the variations of non-uniformity and perpendicularity at the duct outlet (i.e. Plane 6). As the flow-rate increases, the non-uniformity gradually increases, reaches a peak at $Q = 10$ m³/h and then shows a very slight decrease. The non-uniformity represents the difference between the local z-velocity and the averaged z-velocity, indicating the velocity fluctuations in z-direction. As shown in Fig. 19, fluctuations of the z-velocity component present high values at the lower part of Plane 6 and the high-value region is enlarged from $Q = 2$ m³/h to $Q = 10$ m³/h. From Fig. 19f–h, the velocity difference shows a similar distribution, causing a similar non-uniformity.

Figure 20 shows the distributions of V_{xy}/V_z at the duct outlet (i.e. Plane 6), There is an increasing high-value region of xy-velocity component (V_{xy}/V_z) from $Q = 2$ m³/h to $Q = 8$ m³/h, and the distribution is similar during $Q = 10$–25 m³/h. The angle ($90° - \arctan(V_{xy}/V_z)$) is shown in Fig. 21. The angle of 90° indicates that the local velocity is perpendicular to Plane 6. The red region in Fig. 21 corresponding to the large angle (i.e., $90° - \arctan(V_{xy}/V_z)$) gradually decreases to a minimum at $Q = 6$ m³/h and then exhibits similar distributions during $Q = 10$–25 m³/h. As a result, the perpendicularity at Plane 6 decreases firstly to a minimum value at $Q = 6$ m³/h and then gradually increases from $Q = 10$ m³/h to $Q = 25$ m³/h, as depicted in Fig. 18.

5 Concluding remarks

The intake duct is essential in the waterjet propulsion system, which inhales water from the hull bottom and provide it to the waterjet pump. The intake duct is strongly connected with the performance of the waterjet pump and even the complete waterjet propulsion system. This paper aims to shed light on the internal flow features inside the intake duct and reveal the hydraulic loss mechanism under the mooring conditions (zero vessel speed). The planar velocity fields are measured at the duct midplane by using the PIV technique,
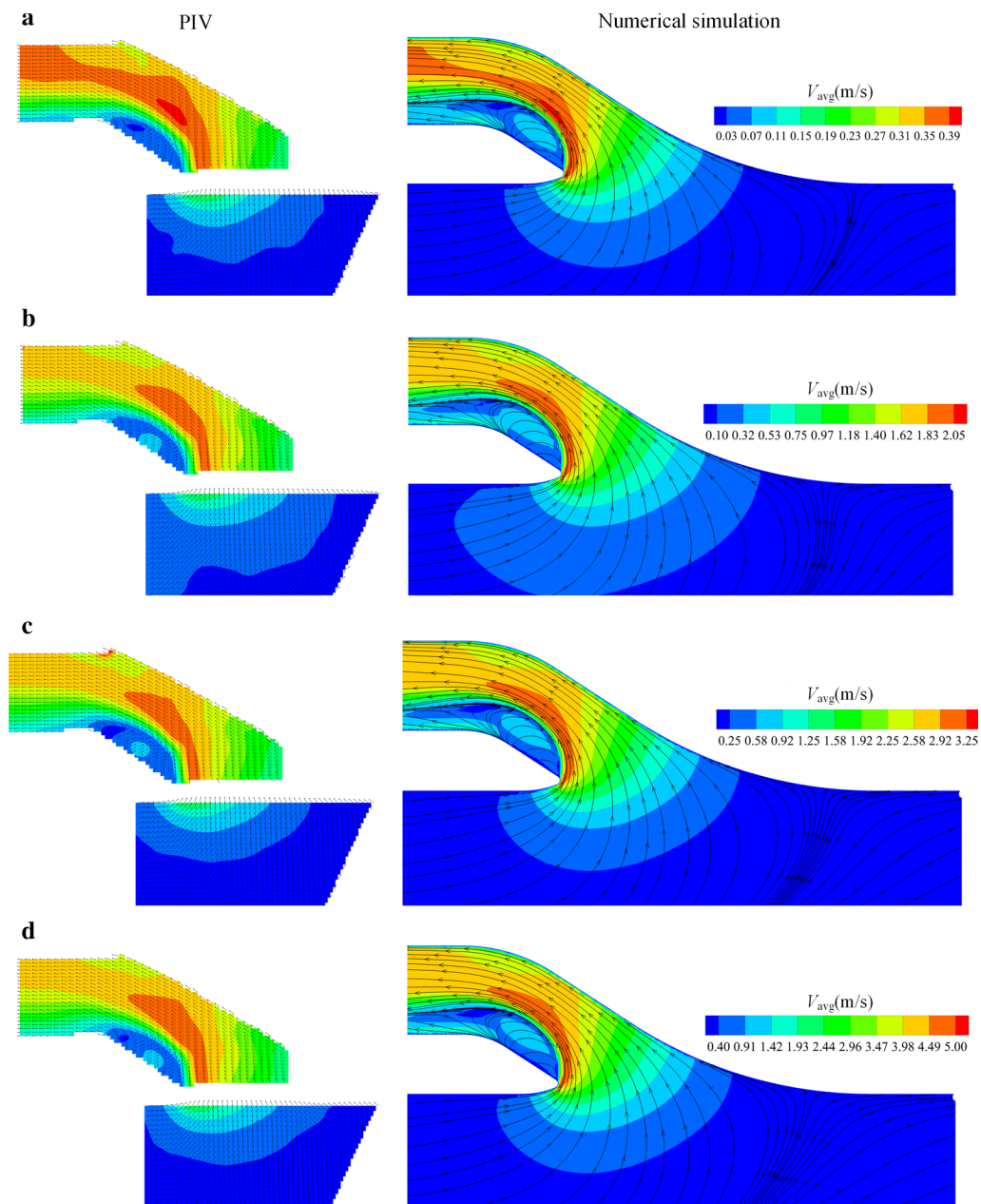
Fig. 15 Comparisons of the velocity fields obtained by the PIV technique (left) and the numerical simulations (right). **a** $Q = 2$ m³/h, **b** $Q = 10$ m³/h, **c** $Q = 16$ m³/h, **d** $Q = 25$ m³/h
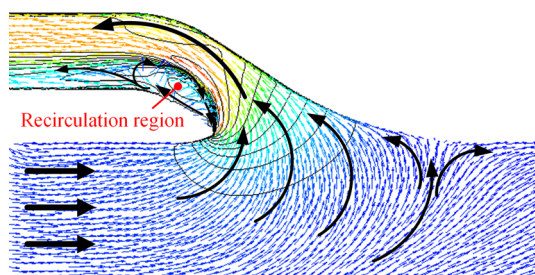

Fig. 16 Flow patterns at the midplane of the intake duct ($Q = 16$ m³/h)

pressures on the duct upper wall are collected through two pressure transducers, and then three-dimensional flow patterns are simulated by using the RNG k-ε turbulence model with the scalable wall function. Based on analyses of the flow features at the midplane and various cross-sections, some conclusions can be drawn:

(1) As the flow-rate increases, the hydraulic loss is gradually increased. According to analyses via the Bernoulli equation, the hydraulic loss h_w is composed of the fric-
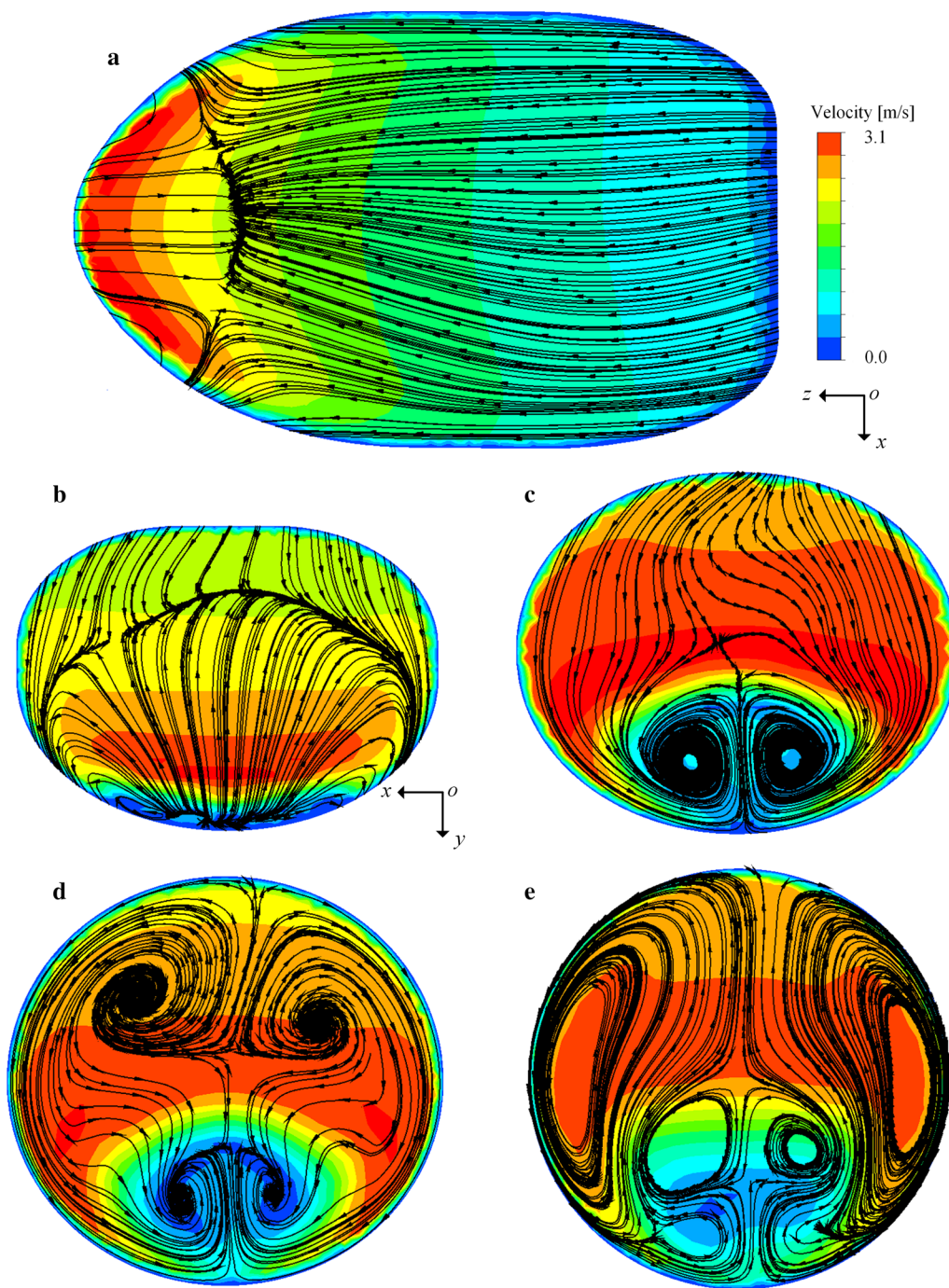
Fig. 17 Velocity fields and streamlines at Plane 1–Plane 5 ($Q = 16$ m^3/h). **a** Plane 1, **b** Plane 2, **c** Plane 3, **d** Plane 4, **e** Plane 5

tional head loss ($h_f \sim V^{1.75}$) and the local head loss ($h_j \sim V^{2.0}$).

(2) Both experimental measurements and numerical simulations mutually demonstrate the flow features at the duct midplane. Outside the intake duct, the fluid is mainly inhaled from lower left side below the intake duct. Subsequently, the fluid strikes the hull upper right wall, coming into two streams with a stagnation
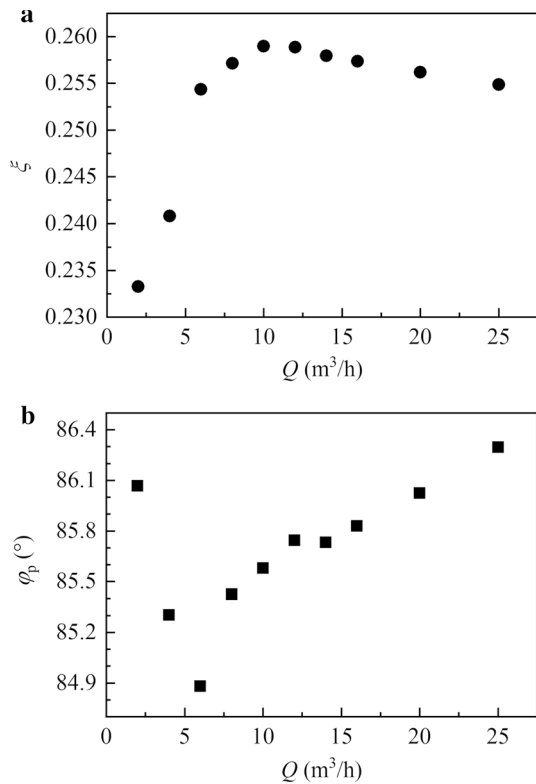
Fig. 18 a Non-uniformity and **b** perpendicularity at the duct outlet, i.e. Plane 6

is drawn into the duct and the other continually moves towards the right side. Inside the intake duct, the suction flow is separated into a recirculation region near the duct lower wall and a high-velocity flow near the upper wall. Finally, a shear flow presents in the horizontal straight pipe with an obvious velocity gradient.

(3) The velocity distribution is axisymmetric at five cross-sections. A vortex pair is observed in the inclined straight section due to the existence of the recirculation region. Subsequently, when the flow strikes the duct upper wall, two vortex pairs are observed in the elbow, and then the flow is strongly turbulent in the horizontal straight pipe. Three-dimensional numerical results demonstrate that the vortex pair is very strong in the recirculation region and then it gradually decreases as the fluid flows downstream.

(4) With the flow-rate increasing, the non-uniformity at the duct outlet gradually increases to a peak at $Q = 10$ m³/h and then slightly decreases during $Q = 10$–25 m³/h. Besides, the perpendicularity at the duct outlet dramatically decreases to a minimum at $Q = 6$ m³/h and then increases as the flow-rate increases.
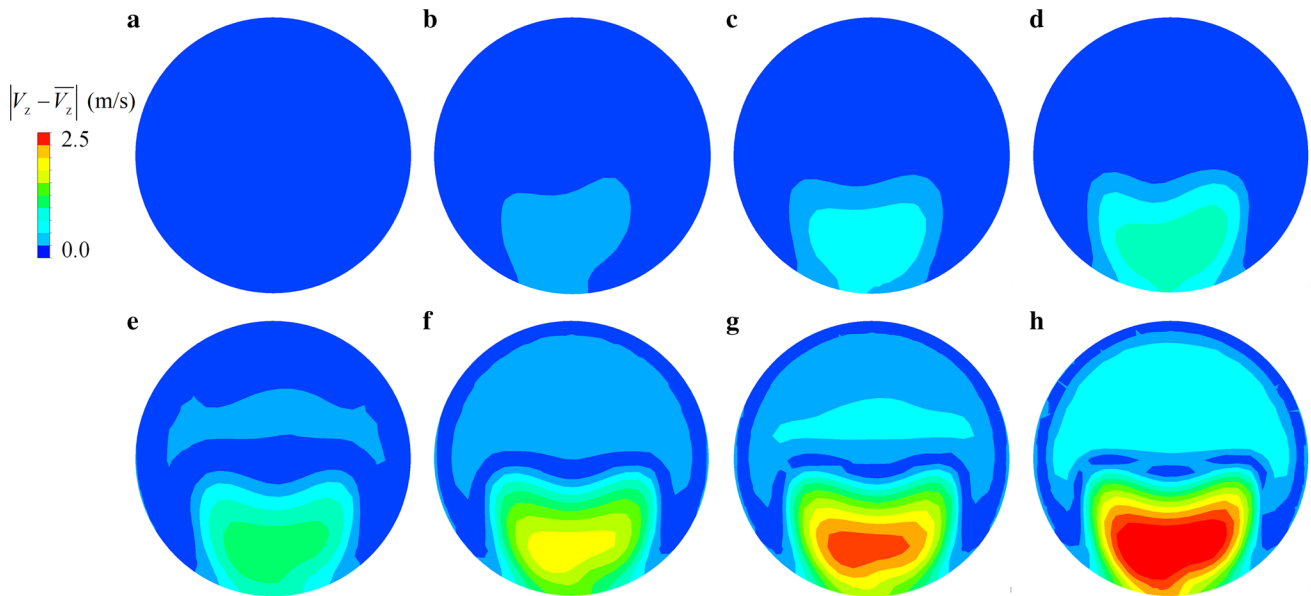

Fig. 19 Fluctuations of z-velocity component $\left(\left|V_z - \overline{V_z}\right|\right)$ at the duct outlet, i.e. Plane 6. **a** $Q = 2$ m³/h, **b** $Q = 4$ m³/h, **c** $Q = 6$ m³/h, **d** $Q = 8$ m³/h, **e** $Q = 10$ m³/h, **f** $Q = 16$ m³/h, **g** $Q = 20$ m³/h, **h** $Q = 25$ m³/h

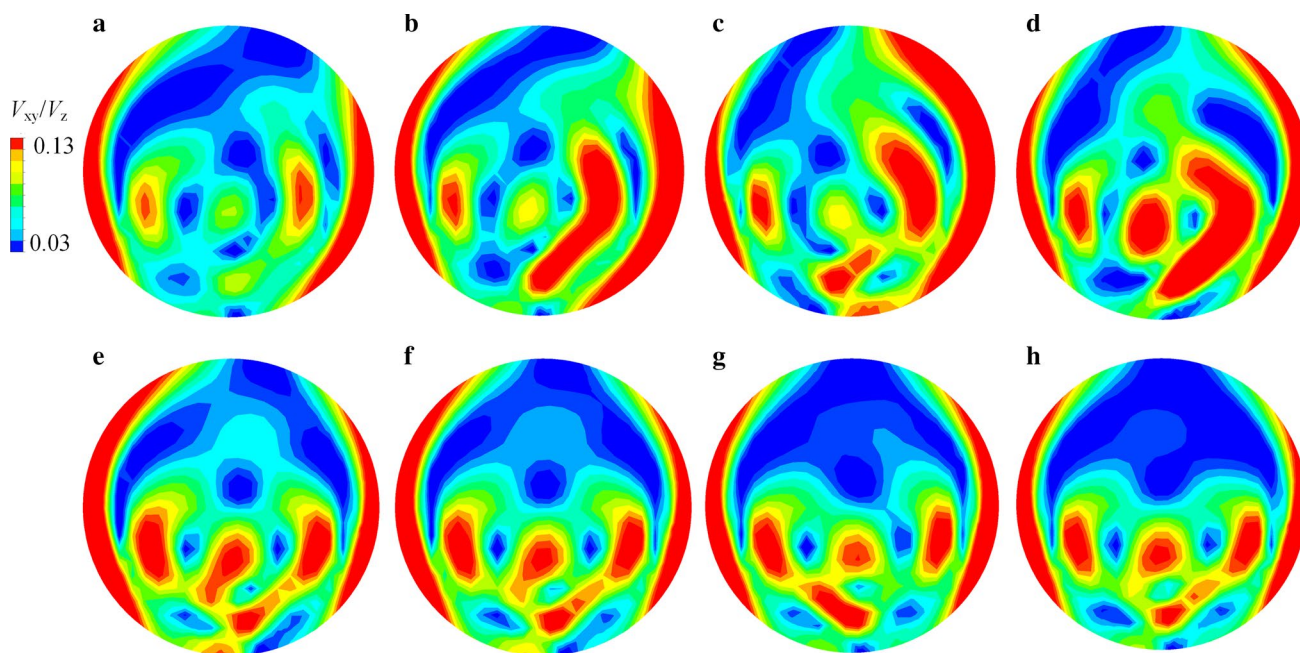point. Two streams are in the opposite directions, one

Fig. 20 Distributions of *xy*-velocity component (V_{xy}/V_z) at the duct outlet, i.e. Plane 6. **a** $Q = 2$ m³/h, **b** $Q = 4$ m³/h, **c** $Q = 6$ m³/h, **d** $Q = 8$ m³/h, **e** $Q = 10$ m³/h, **f** $Q = 16$ m³/h, **g** $Q = 20$ m³/h, **h** $Q = 25$ m³/h

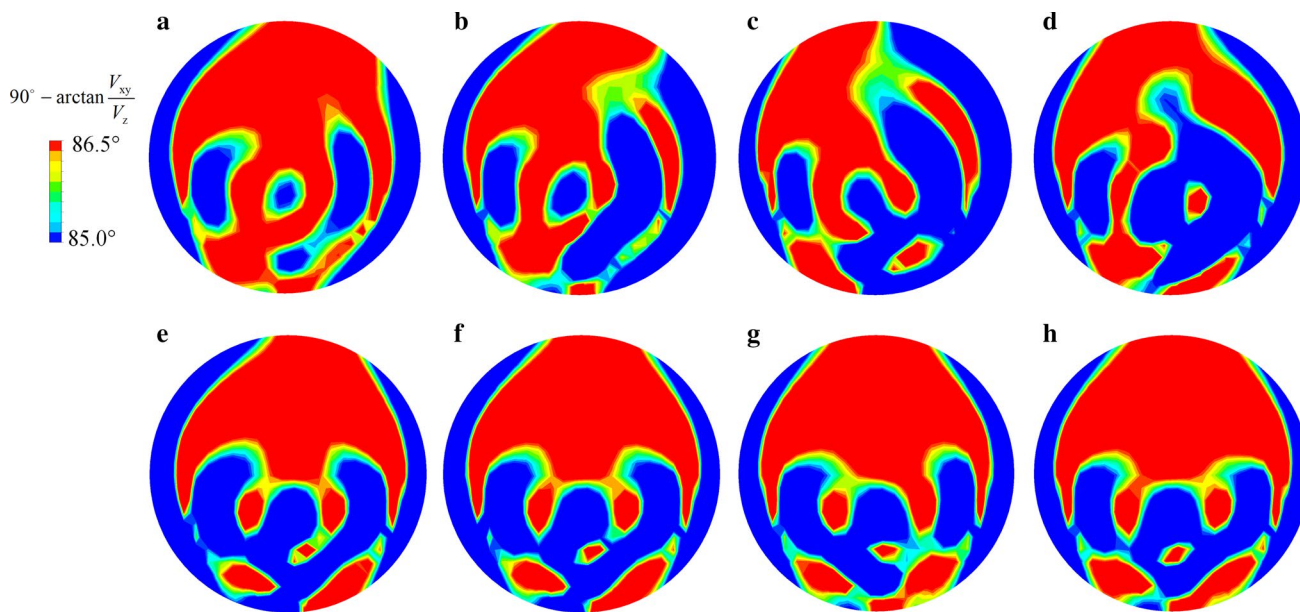**Fig. 21** Distributions of the angle ($90° - \arctan(V_{xy}/V_z)$) at the duct outlet, i.e. Plane 6. **a** $Q = 2$ m³/h, **b** $Q = 4$ m³/h, **c** $Q = 6$ m³/h, **d** $Q = 8$ m³/h, **e** $Q = 10$ m³/h, **f** $Q = 16$ m³/h, **g** $Q = 20$ m³/h, **h** $Q = 25$ m³/h

References

1. Huang, R.F., Dai, Y.X., Luo, X.W., et al.: Multi-objective optimization of the flush-type intake duct for a waterjet propulsion system. Ocean Eng. **187**, 106172 (2019)
2. Park, W.G., Yun, H.S., Chun, H.H., et al.: Numerical flow simulation of flush type intake duct of waterjet. Ocean Eng. **32**, 2107–2120 (2005)
3. Zhu, R., Cao, P., Wang, Y., et al.: Multi-objective hydraulic optimization on intake duct of water-jet propulsion using NSGA-II. In: Proceedings of the ASME-JSME-KSME 2019 8th Joint Fluids Engineering Conference. San Francisco, California, USA. July 28–August 1 (2019)
4. Huang, R.F., Ye, W.X., Dai, Y.X., et al.: Investigations into the unsteady internal flow characteristics for a waterjet propulsion system at different cruising speeds. Ocean Eng. **203**, 107218 (2020)
5. Verbeek R., Bulten N.W.H.: Recent development in waterjet design. In: Proceedings of International Conference on Waterjet Propulsion II, RINA. Amsterdam, Netherlands (1998)
6. Eslamdoost, A., Larsson, L., Bensow, R.: A pressure jump method for modeling waterjet/hull interaction. Ocean Eng. **88**, 120–130 (2014)
7. Gong, J., Guo, C., Wang, C., et al.: Analysis of waterjet-hull interaction and its impact on the propulsion performance of a four-waterjet-propelled ship. Ocean Eng. **180**, 211–222 (2019)
8. Hao, J.F., Zhang, M.D., Huang, X.: The influence of surface roughness on cloud cavitation flow around hydrofoils. Acta Mech. Sin. **34**, 10–21 (2017)
9. Hong, J.R., Abraham, A.: Snow-powered research on utility-scale wind turbine flows. Acta Mech. Sin. **36**, 339–355 (2020)
10. Wang, W., Tang, T., Zhang, Q.D., et al.: Effect of water injection on the cavitation control: experiments on a NACA66 (MOD) hydrofoil. Acta Mech. Sin. **36**, 999–1017 (2020)
11. Griffith-Jones, G.J.: Investigation of incompressible flow through an intake duct with applications to waterjet propulsion. University of Canterbury, Christchurch (1994)
12. Roberts J.L.: The influence of hull boundary layers on waterjet intake performance. University of Tasmania (1998)
13. Jung, K.H., Kim, K.C., Sang, Y.Y., et al.: Investigation of turbulent flows in a waterjet intake duct using stereoscopic PIV measurements. J. Mar. Sci. Technol. **11**, 270–278 (2006)
14. Van Esch, B.P.M.: Performance and radial loading of a mixed-flow pump under non-uniform suction flow. J. Fluids Eng. Trans. ASME **131**, 0511011–0511017 (2009)
15. Zhao, X.L., Sun, Z.X.: A new method for numerical simulation of two trains passing by each other at the same speed. J. Hydrodyn. **22**, 697–702 (2010)
16. Ye, W., Luo, X., Huang, R., et al.: Investigation of flow instability characteristics in a low specific speed centrifugal pump using a modified partially averaged Navier-Stokes model. Proc. Inst. Mech. Eng. Part A: J. Power Energy **233**, 834–848 (2019)
17. Yang, D.D., Luo, X.W., Liu, D.M., et al.: Unstable flow characteristics in a pump-turbine simulated by a modified partially-averaged Navier-Stokes method. Sci. China Technol. Sci. **62**, 406–416 (2019)
18. Luo, X., Ye, W., Huang, R., et al.: Numerical investigations of the energy performance and pressure fluctuations for a waterjet pump in a non-uniform inflow. Renew. Energy **153**, 1042–1052 (2020)
19. Wang, G.Y., Wu, Q., Huang, B.: Dynamics of cavitation-structure interaction. Acta Mech. Sin. **33**, 685–708 (2017)
20. Li, Z.J., Du, Z.B., You, X.C., et al.: Numerical study on dynamic mechanism of brain volume and shear deformation under blast loading. Acta Mech. Sin. **35**, 1104–1119 (2019)
21. Divsalar, K.: Improving the hydrodynamic performance of the SUBOFF bare hull model: a CFD approach. Acta Mech. Sin. **36**, 44–56 (2020)
22. Chen, Q., Liu, Y., Wu, Q., et al.: Global cavitation patterns and corresponding hydrodynamics of the hydrofoil with leading edge roughness. Acta Mech. Sin. **36**, 1202–1214 (2020)
23. Long, Y., Long, X., Ji, B.: LES investigation of cavitating flows around a sphere with special emphasis on the cavitation–vortex interactions. Acta Mech. Sin. **36**, 1238–1257 (2020)
24. Bulten N.W.H.: Numerical analysis of a waterjet propulsion system (2006)
25. Park, W.G., Jang, J.H., Chun, H.H., et al.: Numerical flow and performance analysis of waterjet propulsion system. Ocean Eng. **32**, 1740–1761 (2005)
26. Young Y., Savander B., Kramer M.: Numerical investigation of the impact of SES-Waterjet interactions and flow non-uniformity on pump performance. In: Proceedings of 11th International Conference on Fast Sea Transportation, Honolulu, Hawaii, USA (2011)
27. Duerr P., von Ellenrieder K.: Investigation of non-uniform Waterjet pump inflow for a range of ship speeds. In: Proceedings of Oceans 2013 MTS/IEEE San Diego Conference, San Diego, United States, September 23–26 (2013)
28. Cao, P., Wang, Y., Kang, C., et al.: Investigation of the role of non-uniform suction flow in the performance of water-jet pump. Ocean Eng. **140**, 258–269 (2017)
29. Huang R., Luo X.: Numerical investigation of an intake duct for a waterjet propulsion system using modified partially averaged Navier-Stokes method. In: Proceedings of the ASME-JSME-KSME 2019 8th Joint Fluids Engineering Conference. Volume 3A: Fluid Applications and Systems. San Francisco, California, USA. July 28–August 1 (2019)
30. Guo, J., Chen, Z., Dai, Y.: Numerical study on self-propulsion of a waterjet propelled trimaran. Ocean Eng. **195**, (2020)
31. Zhao, X., Liu, T., Huang, B., et al.: Combined experimental and numerical analysis of cavitating flow characteristics in an axial flow waterjet pump. Ocean Eng. **209**, (2020)
32. Gong, J., Liu, J.G., Dai, Y.X., et al.: Dynamics of stabilizer fins on the waterjet-propelled ship. Ocean Eng. **222**, (2021)
33. Jiang, J., Ding, J.: The hull-waterjet interaction of a planing trimaran. Ocean Eng. **221**, (2021)
34. Wang, S., Wang, Y., Jin, S., et al.: Effect of inlet grid on duct flow performance and waterjet propulsion performance. Jixie Gongcheng Xuebao/J. Mech. Eng. **49**, 164–169 (2013)
35. Luo, C., Cheng, L., Liu, C.: Numerical simulation on the performance of waterjet propulsion system with the protecting grid for different setting angles. J. Yangzhou Univ. Nat. Sci. Ed. **18**, 65–69 (2015)
36. Liu, R., Huang, G.: Numerical study on effect of inlet lip on hydrodynamics for waterjet propulsion. Shipbuilding of China **52**, 39–45 (2011) (in Chinese)
37. Ji, G., Cai, Y., Li, N., et al.: Influence of lip parameters on non-uniformity and stagnation point at inlet duct of waterjet propulsion. Ship Build. China **57**, 109–115 (2016)
38. Ji, G.R., Cai, Y.L., Li, N., et al.: Analysis about affect of inclination angle on the efficiency of the waterjet propulsion inlet duct. Ship Sci. Technol. **38**, 55–58 (2016)
39. Ding, J., Wang, Y.: Research on the parametric design of an inlet duct found in a marine waterjet. Harbin Gongcheng Daxue Xuebao/J. Harbin Eng. Univ. **32**, 423–427 (2011)

40. Guo, J., Zhang, Y., Chen, Z., et al.: CFD-based multi-objective optimization of a waterjet-propelled trimaran. Ocean Eng. **195**, (2020)

41. Smith, L.M., Woodruff, S.L.: Renormalization-group analysis of turbulence. Annu. Rev. Fluid Mech. **30**, 275–310 (1998)

42. Long, Y., Long, X.P., Ji, B., et al.: Verification and validation of URANS simulations of the turbulent cavitating flow around the hydrofoil. J. Hydrodyn. **29**, 610–620 (2017)

43. Huang, R.F., Shao, S.Y., Arndt, R.E.A., et al.: Numerical study of the behaviors of ventilated supercavities in a periodic gust flow. J. Fluids Eng.-Trans. ASME (2020). https://doi.org/10.1115/1.4046110

44. Zhao, Z., He, J.: Hydraulics. Tsinghua University Press, Beijing (2005)